JAERI-M
89-088

ENERGY CONVERSION EFFICIENCY IN HIGH CURRENT RAMAN REGIME FREE ELECTRON LASER (FEL)

I. SINGLE MODE ANALYSIS

July 1989

Yasuaki KISHIMOTO, Hisako ODA*, Makoto SHIHO
Kazuo ODAJIMA and Hikosuke MAEDA

日本原子力研究所
Japan Atomic Energy Research Institute

JAERI-Mレポートは，日本原子力研究所が不定期に公刊している研究報告書です。
入手の問合わせは，日本原子力研究所技術情報部情報資料課（〒319-11茨城県那珂郡東海村）あて，お申しこしください。なお，このほかに財団法人原子力弘済会資料センター（〒319-11 茨城県那珂郡東海村日本原子力研究所内）で複写による実費頒布をおこなっております。

JAERI-M reports are issued irregularly.
Inquiries about availability of the reports should be addressed to Information Division Department of Technical Information, Japan Atomic Energy Research Institute, Tokai-mura, Naka-gun, Ibaraki-ken 319-11, Japan.

©Japan Atomic Energy Research Institute, 1989

編集兼発行　日本原子力研究所
印　　刷　いばらき印刷㈱

JAERI-M 89-088

Energy Conversion Efficiency in High Current Raman Regime Free Electron Laser (FEL) I. Single Mode Analysis

Yasuaki KISHIMOTO, Hisako ODA*, Makoto SHIHO
Kazuo ODAJIMA and Hikosuke MAEDA

Department of Thermonuclear Fusion Research
Naka Fusion Research Establishment
Japan Atomic Energy Research Institute
Naka-machi, Naka-gun, Ibaraki-ken

(Received June 20, 1989)

The effect of the longitudinal electrostatic field on the energy conversion efficiency is investigated by use of a 1-dimensional FEL amplification code. It is found that the repulsive electrostatic interaction prevents the periodic bounce motion of trapped electrons in the ponderomotive potential especially in the high current Raman operation regime. The irregular rotation of the trapped electron increases the untrapped ones, which obtained the kinetic energy from the radiation field. Resultantly, the energy conversion efficiency averaged over a long wiggler distance stays in a lower level than that predicted by the trapping argument. It is also found that the finite beam energy spread reduces the electrostatic force in the nonlinear trapping stage. The reduction of the electrostatic force recovers the periodic electron bounce motion and the associated amplitude oscillation of the radiation field.

Keywords: Raman FEL, Relativistic Electron Beam, Induction Linac, Conversion Efficiency, Electrostatic Interaction, Helical Wiggler

---

* Kanazawa Computer Service Corp.

JAERI－M 89－088

高電流ラマン領域自由電子レーザー（FEL）におけるエネルギー変換効率
Ⅰ．単一モード解析

日本原子力研究所那珂研究所核融合研究部
岸本　泰明・小田　久子*・志甫　　諒
小田島和男・前田　彦祐

（1989年6月20日受理）

1次元自由電子レーザー（FEL）増幅コードを用いて，エネルギー変換効率に対する縦方向の静電場の効果が調べられた。粒子間に反作用を及ぼす静電相互作用は，特に高電流ラマン動作領域において，動重力ポテンシャル中での捕捉電子の周期的な施回運動を妨たげることがわかった。捕捉電子の不規則な回転は，輻射場から運動エネルギーを持ち去る非捕捉電子を増加させる。その結果，長いウィグラー長に渡って平均化されたエネルギー変換効率は，捕捉理論から予測される値よりも低い値に止まる。さらに，有限なビームのエネルギー広がりは，非線形の強い捕捉状態では静電力を抑制することがわかった。静電力の減衰は，周期的な電子の施回運動とそれに付随する輻射場の振幅振動を回復させる。

那珂研究所：〒311－01 茨城県那珂郡那珂町大字向山801－1
＊（株）カナザワコンピューターサービス

Contents

目　　次

1. Introduction

Recently, high power wave generation in the range of millimeter wavelength has been extensively investigated by use of the Free Electron Laser(FEL)[1,2]. One of important key issues of FEL is the energy conversion efficiency from a relativistic electron beam energy to a radiation field energy. Theoretical investigation, i.e. the trapping argument, indicates that a maximum conversion efficiency after the saturation of a linear growth of the radiation field increases with a beam current density I_b according to the relation $\eta \propto I_b^{1/3}$ for a fixed beam energy E_b [3,4]. Numerical simulations also show the above relation in a weak current Compton regime where the electrostatic beam mode is less important[5,6]. However, the current dependence of the conversion efficiency in a high current Raman regime is not systematically examined. In the Raman operation regime, FEL amplification is characterized by the electrostatic beam mode excitation. That is, the longitudinal electrostatic potential Φ_{es} modulates the ponderomotive potential Φ_p and affects a linear growth rate of the radiation field. Since the electrostatic force $f_{es}(\equiv \partial\Phi_{es}/\partial z)$ becomes comparable to the ponderomotive bunching force $f_p(\equiv \partial\Phi_p/\partial z)$ with increasing a beam current density, the energy conversion efficiency should be determined by taking into account the detailed behaviour of electrons which are influenced by the electrostatic field. T.M. Antonsen recently pointed out an importance of the electrostatic field in a tapered wiggler FEL[7]. He analytically found that the repulsive electrostatic field leads the particle spilling from a ponderomotive potential well and a deceleration rate of the wiggler parameter is limited to obtain the high energy conversion efficiency.

In the paper, we analytically derive the ratio between the electrostatic force f_{es} and the ponderomotive one f_p, i.e. f_{es}/f_p. It is found that the electrostatic force f_{es} closely related to the electron phase and/or the electron distribution in a ponderomotive potential well and plays an

important role in the nonlinear trapping stage even if f_{es} is small compared with f_p in the linear stage. In order to examine the above effect, we investigate the particle dynamics in the wiggler field over the wide range from the lower current Compton regime to the higher current Raman one by using a 1-dimensional FEL amplification code, where the electrostatic interaction is taken into account. Here, we introduce a conversion efficiency averaged over the long wiggler distance $\langle\eta\rangle$ as a realistic parameter, in addition to a maximum conversion efficiency η_{max} which is used in the usual FEL analysis[3-6]. It is found that the longitudinal electrostatic interaction prevents the regular periodic bounce motion of the bunched electron in a ponderomotive potential well especially in the high current Raman regime and suppresses the amplitude oscillation of the saturated radiation power. Resulatantly, an averaged conversion efficiency $\langle\eta\rangle$ stays in a lower level than that expected from the trapping argument. We also analyze the effect of the axial beam energy spread. We find that the finite axial beam energy spread plays a role to reduce the electrostatic force.

In 2, we derive an analytical expression for f_{es}/f_p to estimate the magnitude of the electrostatic force. Basic equations for the numerical calculation and numerical methods are described in 3. In 4, results of numerical analyses are presented and discussed. The effect of the axial energy spread is also discussed in 4-2. §5 summarizes our conclusions.

2. Analytical Estimate for f_{es}/f_p in Trapping Stage

The physical model we employ here is the 1-dimensional relativistic electron beam interacting with the spatially periodic helical wiggler field, the radiation field and the space charge field, which are described by using the vector and scalar potentials as follows

important role in the nonlinear trapping stage even if f_{es} is small compared with f_p in the linear stage. In order to examine the above effect, we investigate the particle dynamics in the wiggler field over the wide range from the lower current Compton regime to the higher current Raman one by using a 1-dimensional FEL amplification code, where the electrostatic interaction is taken into account. Here, we introduce a conversion efficiency averaged over the long wiggler distance $\langle\eta\rangle$ as a realistic parameter, in addition to a maximum conversion efficiency η_{max} which is used in the usual FEL analysis[3-6]. It is found that the longitudinal electrostatic interaction prevents the regular periodic bounce motion of the bunched electron in a ponderomotive potential well especially in the high current Raman regime and suppresses the amplitude oscillation of the saturated radiation power. Resulatantly, an averaged conversion efficiency $\langle\eta\rangle$ stays in a lower level than that expected from the trapping argument. We also analyze the effect of the axial beam energy spread. We find that the finite axial beam energy spread plays a role to reduce the electrostatic force.

In 2, we derive an analytical expression for f_{es}/f_p to estimate the magnitude of the electrostatic force. Basic equations for the numerical calculation and numerical methods are described in 3. In 4, results of numerical analyses are presented and discussed. The effect of the axial energy spread is also discussed in 4-2. §5 summarizes our conclusions.

2. Analytical Estimate for f_{es}/f_p in Trapping Stage

The physical model we employ here is the 1-dimensional relativistic electron beam interacting with the spatially periodic helical wiggler field, the radiation field and the space charge field, which are described by using the vector and scalar potentials as follows

$$A_w(z)=-A_w(e_x\cos k_w+e_y\sin k_w z), \tag{1}$$

$$A_s(z,t)=A_s(z)\left\{e_x\cos\left[\int_0^z k_+(z')-\omega t\right]dz'-e_y\sin\left[\int_0^z k_+(z')-\omega t\right]dz',\right. \tag{2}$$

$$\Phi_{es}(z,t)=\Phi(z)\cos\left[\int_0^z k(z')-\omega t\right]dz', \tag{3}$$

where k_w and $A_0(=B_w/k_w)$ are the wave number and the amplitude of the helical wiggler field, and are taken to be constant in the analysis of this section. $A_s(z)$ and $\Phi(z)$ are slowly varying part of the vector and scalar potentials, $k_+(z)$ and $k(z)$ are corresponding wave numbers, and ω is the wave frequency.

The Hamiltonian of such a particle is given by

$$H=\left\{m^2c^4+c^2p_z^2+e^2[A_0(z)+A_s(z,t)]^2\right\}^{1/2}-e\Phi(z,t), \tag{4}$$

where p_z is the canonical momentum in an axial direction. In Eq.(4), zero transverse canonical momentum, i.e. $p_\perp=0$, is assumed. The axial equation of motion for an electron is obtained from Eq.(4) as $dp_z/dz=f_p+f_{es}$, where $f_p\equiv e\partial\Phi_p/\partial z$ and $f_{es}\equiv e\partial\Phi_{es}/\partial z$. The ponderomotive force f_p is given by

$$f_p = -\frac{e^2A_0}{\gamma mc^2}\frac{\partial}{\partial z}[\,A_s(z)\cos\psi(z,t)\,], \tag{5}$$

where $\gamma mc^2\equiv(1-v^2/c^2)^{-1/2}$ is the total kinetic energy of an electron and $\psi(z,t) = \int_0^z[k_+(z')+k_w]dz'-\omega t$ represents an electron phase with respect to the ponderomotive potential. In deriving Eq.(5), we assume the condition $A_0\gg A_s$. The electrostatic force f_{es} is derived from Eq.(3) as

$$f_{es} = e\frac{\partial\Phi_{es}}{\partial z}=e\frac{\partial\Phi}{\partial z}\cos\psi_1-k(z)\Phi(z)\sin\psi_1, \tag{6}$$

where $\psi_l(z,t)=\int_0^z k(z')dz'-\omega t$ represents an electron phase with respect to the electorostatic field. In Eq.(6), $\partial\Phi/\partial z$ and $\Phi(z)$ are evaluated from the Poisson equation described by Coulomb gauge ;

$$\frac{\partial^2\Phi_{es}}{\partial z\partial t}=\omega\left[\frac{\partial\Phi}{\partial z}\sin\psi_l+k(z)\Phi(z)\cos\psi_l\right]=4\pi J_z(z,t), \tag{7}$$

where $J_z(z,t)$ is the axial beam current density given by

$$J_z(z,t)=-\frac{en_bL}{N_T}\sum_{j=1}^{N}\delta[\ t-\tau_j(z,t_{j0})\ ]\frac{v_j(z,t_{j0})}{|v_{zj}(z,t_{j0})|}.$$

Here, N_T is the total number of electron within an interaction region of length L and n_b denotes the electron beam density. $\tau_j(z,t_{j0})$ represents the time of j-th electron at position z which entered the interaction region at time t_{j0}, i.e. $\tau_j=t_{j0}+\int_0^z dz'/v_{zj}(z',t_{j0})$. Then, electron phases, ψ and ψ_l, are given by

$$\psi(z,t)\ =\ \psi_0\ +\ \int_0^z\left[\ k_+(z')+k_w-\frac{\omega}{v_z(z')}\ \right]dz', \tag{8}$$

$$\psi_l(z,t)\ =\ \psi_0\ +\ \int_0^z\left[\ k(z')-\frac{\omega}{v_z(z')}\ \right]dz', \tag{9}$$

where $\psi_0=-t_0\omega$ denotes the initial electron phase. Assuming the periodicity with respect to the time interval $T=2\pi/\omega$, we average Eq.(10) over the time interval T and obtain equations for $\partial\Phi/\partial z$ and $k\Phi$ as follows

$$\frac{\partial\Phi}{\partial z}\ =\ -\frac{2\omega^2_Em}{e\omega}\langle v_{z0}\sin\psi_l\rangle, \tag{10}$$

$$k\phi = -2\frac{\omega_b^2}{\omega c^2}\langle v_{z0}\cos\psi_1\rangle . \tag{11}$$

Here, $\omega_b=(4\pi n_b e^2/m)^{1/2}$ is the plasma frequency and v_{z0} represents an axial electron velocity at $t=t_{j0}$. In Eqs.(10) and (11), $\langle\ \ \rangle$ denotes an average over the initial beam momentum distribution $f_b(p_0)$ and the initial electron phase ψ_0 which is defined by

$$\langle\ (\ldots)\ \rangle=\frac{1}{2\pi n_b}\int_{-\pi}^{\pi}d\psi_0\int f_b(p_0)(\ldots)dp_0. \tag{12}$$

Then, Eq.(6) is rewritten by employing Eqs.(10) and (11) as

$$f_{es} = \frac{2\omega_b^2 m}{\omega}[\ \sin\psi_1\langle\cos\psi_1\rangle-\cos\psi_1\langle\sin\psi_1\rangle\ ]. \tag{13}$$

Assuming that the amplitude of the radiation field as well as the electrostatic field varies slowly, satisfying conditions $|\partial\psi/\partial z| \gg |\partial\ln a_s/\partial z|$ and $|\partial\psi_1|/\partial z \gg |\partial\ln\phi_{es}/\partial z|$, we estimate the ratio $|f_{es}/f_p|$ as

$$\left|\frac{f_s}{f_p}\right| = \frac{2\xi^2\gamma^2k_w^2c\delta}{a_0a_s\omega(k_+ + k_w)}|H(\psi,\psi_1)|, \tag{14}$$

where $|H(\psi,\psi_1)|$ represents the phase factor given by

$$H(\psi,\psi_1) = \frac{\sin\psi_1}{\sin\psi}\langle\beta_{z0}\cos\psi_1\rangle. \tag{15}$$

Here, $a_0(=eA_0/mc^2)$, $a_s(=eA_s/mc^2)$ and $\phi(=e\Phi/mc^2)$ are normalized vector and

scalar potentials. $\xi=\omega_b/\gamma_b^{1/2}ck_w$ is the normalized plasma frequency ($\gamma_b=\gamma(t=t_0)$), and $\beta_{z0}=v_{z0}/c$. In Eq.(15), we introduce the trapping fraction δ due to the ponderomotive potential by assuming that the contribution from untrapped particles to the phase factor $H(\psi,\psi_1)$ is negligibly small. N.M.Kroll et al[8] derived a similar relation as Eq.(14). Their result, however, does not include the phase factor $H(\psi,\psi_1)$, which is important to determine the elecrostatic force in the nonlinear trapping stage.

It is found in Eq.(14) that the force ratio $|f_{es}/f_p|$ depends not only on the trapped particle density $n_b\delta$ and the radiation field amplitude a_s, but also on the particle distribution in the ponderomotive potential well, i.e. $H(\psi,\psi_1) \simeq \langle \cos\psi_1 \rangle$(assuming $\psi_1\simeq\psi$ and $\beta_{z0}\simeq1$). For example, the phase factor H becomes $H\simeq0$ for randomly distributed trapped particles in $-\pi\leq\psi_1\leq\pi$ and $H\simeq\pi/2$ for the same trapped particle distribution in $-\pi/2\leq\psi_1\leq\pi/2$. For the bunched electron distribution which is occupied by the small phase space area compared with the bucket of the radiation field, the magnitude of H depends on the phase of the bunched electron. Namely, during one bounce motion, the bunched electron which bounces in the ponderomotive potential well suffers two times strong electrostatic force($H\simeq1$) at around $\psi_1\simeq0$. Note here that the coordinate $\psi_1\simeq0$ for the bunched electron corresponds to the coordinate that the radiation power becomes peak value or the bottom one. In. 4, we investigate the effect of the electrostatic force on the phase space distribution of the bunched electron in addition to the energy conversion efficiency.

3. Basic Equations and Numerical Method

The single mode($\omega=f/2\pi$) 1-dimensional FEL formulation employed here is basically given by H.P.Freund[9] and developed by taking into account the electrostatic interaction and the axial beam energy spread. The averaging procedure in a p_{z0}-direction for the given beam momentum distribution $f_b(p)$

scalar potentials. $\xi=\omega_b/\gamma_b^{1/2}ck_w$ is the normalized plasma frequency ($\gamma_b=\gamma(t=t_0)$), and $\beta_{z0}=v_{z0}/c$. In Eq.(15), we introduce the trapping fraction δ due to the ponderomotive potential by assuming that the contribution from untrapped particles to the phase factor $H(\psi,\psi_1)$ is negligibly small. N.M.Kroll et al[8] derived a similar relation as Eq.(14). Their result, however, does not include the phase factor $H(\psi,\psi_1)$, which is important to determine the elecrostatic force in the nonlinear trapping stage.

It is found in Eq.(14) that the force ratio $|f_{es}/f_p|$ depends not only on the trapped particle density $n_b\delta$ and the radiation field amplitude a_s, but also on the particle distribution in the ponderomotive potential well, i.e. $H(\psi,\psi_1) \simeq \langle \cos\psi_1 \rangle$(assuming $\psi_1\simeq\psi$ and $\beta_{z0}\simeq1$). For example, the phase factor H becomes $H\simeq0$ for randomly distributed trapped particles in $-\pi\leq\psi_1\leq\pi$ and $H\simeq\pi/2$ for the same trapped particle distribution in $-\pi/2\leq\psi_1\leq\pi/2$. For the bunched electron distribution which is occupied by the small phase space area compared with the bucket of the radiation field, the magnitude of H depends on the phase of the bunched electron. Namely, during one bounce motion, the bunched electron which bounces in the ponderomotive potential well suffers two times strong electrostatic force($H\simeq1$) at around $\psi_1\simeq0$. Note here that the coordinate $\psi_1\simeq0$ for the bunched electron corresponds to the coordinate that the radiation power becomes peak value or the bottom one. In. 4, we investigate the effect of the electrostatic force on the phase space distribution of the bunched electron in addition to the energy conversion efficiency.

3. Basic Equations and Numerical Method

The single mode($\omega=f/2\pi$) 1-dimensional FEL formulation employed here is basically given by H.P.Freund[9] and developed by taking into account the electrostatic interaction and the axial beam energy spread. The averaging procedure in a p_{z0}-direction for the given beam momentum distribution $f_b(p)$

in Eq.(12) is performed by means of an 10-th order Gaussian quadrature technique in the variable p_{z0} which permits the small number of test particle to obtain an enough accuracy in the numerical calculation. The slowly varying part of the vector potential, a_s, obeys the following equations ;

$$\frac{\partial^2 a_s}{\partial z^2}+\left(\frac{\omega^2}{c^2}-k_+^2\right)a_s=\frac{\omega_b^2}{c^2}\left\langle\frac{\beta_{z0}}{v_z}\left[v_1\cos\psi-v_2\sin\psi\right]\right\rangle, \tag{16}$$

$$2k_+^{1/2}\frac{\partial}{\partial z}\left(k_+^{1/2}a_s\right)=-\frac{\omega_b^2}{c^2}\left\langle\frac{\beta_{z0}}{v_z}\left[v_1\sin\psi+v_2\cos\psi\right]\right\rangle, \tag{17}$$

where v_1 and v_2 denote the perpendicular velocity of an electron described in a helical coordinate. Note that Eqs.(16) and (17) couple to the Poisson equations given by Eqs.(10) and (11).

Here, we assume that an electron beam is composed of N test particles and particles are uniformly distributed in the phase space in the initial stage. Then, Eqs.(10) and (11), and Eqs.(16) and (17) couple to $3N$ equations of motion given by

$$\frac{dp_1}{dz}=\left(\Omega_0-\frac{k_w p_z}{m}\right)\frac{mp_2}{p_z}+mc\left\{\left(\frac{\gamma m\omega}{p_z}-k_+\right)a_s\sin\phi+\cos\phi\frac{da_s}{dz}\right\}, \tag{18}$$

$$\frac{dp_2}{dz}=\left(\Omega_0-\frac{k_w p_z}{m}\right)\frac{mp_1}{p_z}+mc\left\{\left(\frac{\gamma m\omega}{p_z}-k_+\right)a_s\cos\phi-\sin\phi\frac{da_s}{dz}\right\}-\Omega_w m, \tag{19}$$

$$\frac{dp_z}{dz}=\Omega_w m\frac{p_2}{p_z}+\frac{mc}{p_z}\left\{a_s k_+\left(p_1\sin\psi+p_2\cos\psi\right)-\frac{da_s}{dz}\left(p_1\cos\psi-p_2\sin\psi\right)\right\}$$

$$-\frac{\gamma m^2c^2}{p_z}\left(k\phi\sin\psi_1-\frac{d\phi}{dz}\cos\psi_1\right), \tag{20}$$

where $\Omega_w=eB_w/mc$, and $p_{1,2}=\gamma m v_{1,2}$ is the electron perpendicular momentum. In Eqs.(18) and (19), $\Omega_0=eB_0/mc$ represents the axial guide field for the stable

propagation of the electron beam.

Here, we use the helical wiggler FEL as an amplification system of the f=60GHz microwave[10]. In the following calculation, the beam energy E_b and the wiggler pitch λ_w are fixed to E_b=1MeV (γ_b~2.96) and λ_w=4cm, and the beam current density I_b is taken to the variable parameter. Therefore, according to the beam current density I_b, the wiggler field B_w is determined by solving the linear dispersion relation so as to satisfy the condition for the maximum growth rate of the radiation field[11]. The wiggler field is adiabatically increased in the entry region $0 \leq z \leq 10\lambda_w$ to guide the electron beam to a stable orbit. An initial level of the electrostatic potential, i.e. $\phi(z=0) = -2\omega_b^2 \langle \cos\phi_l \rangle / c^2\omega(k_+ + k_w)$, is determined from the numerical error which corresponds to an initial setting of test particles in the phase space. Here, the initial value of k_+ is also determined from the dispersion relation. In the numerical calculation, about 500 test particles are employed by examining the numerical convergence for the energy conversion efficiency averaged over the long wiggler distance.

4. Numerical Results and Discussions

In 4.1, we show results in the absence of the axial beam energy spread. Effect of the axial energy spread is discussed in 4.2. In the following calculation, the initial input radiation power, $P_{a,in}$, is chosen to $P_{a,in}$=10W/cm^2.

4.1 Case without Axial Beam Energy Spread

Here, we choose the electron momentum distribution in Eq.(12) as $f_b(p_0) = n_b\delta(p_z - p_{z0})\delta(p_x)\delta(p_y)$, where $p_{z0} = \gamma_b m v_{z0}$ ($v_{z0} \equiv (1-\gamma_b^{-2})^{1/2}$). Figure 1 shows the linear growth rate Γ versus the beam current density I_b in the case with the electrostatic field $\phi \neq 0$ (open circles) and without one ϕ=0 (open triangles). The wiggler field B_w is also illustrated in Fig.1. In the

propagation of the electron beam.

Here, we use the helical wiggler FEL as an amplification system of the f=60GHz microwave[10]. In the following calculation, the beam energy E_b and the wiggler pitch λ_w are fixed to E_b=1MeV (γ_b~2.96) and λ_w=4cm, and the beam current density I_b is taken to the variable parameter. Therefore, according to the beam current density I_b, the wiggler field B_w is determined by solving the linear dispersion relation so as to satisfy the condition for the maximum growth rate of the radiation field[11]. The wiggler field is adiabatically increased in the entry region $0 \leq z \leq 10\lambda_w$ to guide the electron beam to a stable orbit. An initial level of the electrostatic potential, i.e. $\phi(z=0) = -2\omega_b^2 \langle \cos\phi_l \rangle / c^2\omega(k_+ + k_w)$, is determined from the numerical error which corresponds to an initial setting of test particles in the phase space. Here, the initial value of k_+ is also determined from the dispersion relation. In the numerical calculation, about 500 test particles are employed by examining the numerical convergence for the energy conversion efficiency averaged over the long wiggler distance.

4. Numerical Results and Discussions

In 4.1, we show results in the absence of the axial beam energy spread. Effect of the axial energy spread is discussed in 4.2. In the following calculation, the initial input radiation power, $P_{a,in}$, is chosen to $P_{a,in}$=10W/cm^2.

4.1 Case without Axial Beam Energy Spread

Here, we choose the electron momentum distribution in Eq.(12) as $f_b(p_0) = n_b\delta(p_z - p_{z0})\delta(p_x)\delta(p_y)$, where $p_{z0} = \gamma_b m v_{z0}$ ($v_{z0} \equiv (1-\gamma_b^{-2})^{1/2}$). Figure 1 shows the linear growth rate Γ versus the beam current density I_b in the case with the electrostatic field $\phi \neq 0$ (open circles) and without one ϕ=0 (open triangles). The wiggler field B_w is also illustrated in Fig.1. In the

calculation, no axial guide field is applied. The transition from the Compton regime to the Raman one is observed around the current density $I_b \simeq 60 A/cm^2 (\equiv I_{bc})$, when the electrostatic field is taken into account[12]. Furthermore, the linear growth rate shows the relation $\Gamma \propto I_b^{1/3}$ for $I_b \lesssim I_{bc}$ and $\Gamma \propto I_b^{1/4}$ for $I_b \gtrsim I_{bc}$, which are predicted from the linear response theory[3,4]. On the other hand, no Raman transition is found in the $\phi=0$ case. The linear growth rate deviates from the above power dependence in the current density region for $I_b \gtrsim 2KA/cm^2$. This is due to the fact that a low frequency mode comes close to a high frequency main mode under consideration and then the wave growth deviates from the ideal case where two modes separates enough. Further increase of the current density for the present wiggler parameters leads the decoupling between an electrostatic beam mode and a electromagnetic one. Therefore, we restrict the current density for $I_b \lesssim 2KA/cm^2$ in the present calculation.

Figure 2(a) illustrates the typical spatial evolution of the radiation power P_a in the case without the electrostatic field for $I_b=1.5KA/cm^2$. Figure 2(b) shows the corresponding trapping efficiency of electrons due to the ponderomotive potential. The trapping efficiency δ is estimated from the separatrix equation $S(\psi, d\psi/dz)=0$, where the function S is defined by

$$S(\psi, \frac{d\psi}{dz}) \equiv \left(\frac{d\psi}{dz} \right)^2 - \frac{8 a_0 a_s k_w^2}{\gamma_\perp^2} (1 + \cos\psi) . \qquad (21)$$

Here, ψ is given by Eq.(8) and $\gamma_\perp = 1 + a_0^2$ ($a_0 = eB_w/mc^2 k_w$) . In deriving Eq.(21), we assume that the radiation amplitude varies slowly enough satisfying the condition $|\partial\psi/\partial z| \gg |\partial \ln a_s/\partial z|$. Conditions, $\gamma^2 \gg \gamma_\perp^2$, $k_+ \gg \xi^2 k_w/2$ and $k_w \gg d\psi/dz$, are also employed. In Eq.(21), $S(\psi, d\psi/dz)<0$ represents a trapped particle and $S(\psi, d\psi/dz)>0$ represents a untrapped one. Furthermore, untrapped particles are divided into two groups as shown in Fig.2(b). One

is an untrapped particle with $d\psi/dz>0$, which we call an "up-scattering particle", hereafter. Such a particle has the axial velocity v_z faster than the phase velocity of the ponderomotive potential $v_p(\equiv\omega/(k_+ + k_w))$. Another one is an untrapped particle with $d\psi/dz<0$, i.e. a "down-scattering one", in which the axial velocity v_z is lower than v_p. As seen in Fig.2(a), the linear growth of the radiation field saturates at around $z=18\lambda_w$ ($\equiv z_{sat}$; saturation coordinate which gives the peak value of the radiation field) and then repeats the amplitude oscillation. Here, we define the averaged value of a local quantity $A(z)$ over the long wiggler distance as

$$\langle A(z)\rangle \equiv \frac{1}{L-z_{sat}}\int_{z_{sat}}^{L} A(z)\,dz, \tag{22}$$

where L is the interaction length and taken to $L=100\lambda_w$ in the present numerical calculation. Then, the averaged radiation power in Fig.2 obtained according to Eq.(22) is evaluated as $\langle P_a\rangle\simeq 2.0\times10^8 W/cm^2$, and the trapping efficiency averaged in a same manner is about $\langle\delta\rangle\simeq 80\%$. Note also in Fig.2(b) that the ratio of the down-scattering particle ($\langle\delta_{down}\rangle\simeq 15\%$) is larger than the up-scattering one ($\langle\delta_{up}\rangle\simeq 5\%$). This feature is also seen in Fig.4 in which the particle positions(represented by dots) and the separatrix(solid line) in phase space $(\psi, d\psi/dz)$ are plotted from $z=15\lambda_w$(linear stage) to $z=35\lambda_w$(trapping stage) corresponding to Fig.2. It is found in the figure that the bunched electrons are shallowly trapped near the separatrix and the deeply trapped particles ($\psi\simeq 0, d\psi/dz\simeq 0$) are not found.

The same spatial evolution as Fig.2 for the $\phi\neq 0$ case is illustrated in Fig.3. Dashed line in Fig.3(a) represents the space charge field ϕ^2. The peak value of P_a, i.e. $P_{a,max}(\equiv P_a(z_{sat}))$, observed at around $z=18\lambda_w$ roughly becomes the same value as the case without the electrostatic field(see Fig.2(a)). It is found, however, that the amplitude oscillation is

suppressed small and the averaged radiation power is reduced to $\langle P_a \rangle \simeq 1.2 \times 10^8 W/cm^2$. The small reduction of the averaged trapping efficiency $\langle \delta \rangle \simeq 76\%$ is also found in Fig.3(b). Furthermore, Fig.3(b) shows that the up-scattering untrapped particles are considerably increased in comparison with the case without the electrostatic field(see Fig.2(b)). These results are explained by investigating the electron behaviour in the phase space(Fig.5) as follows. As explained in 2, the bunched electron suffers the strong electrostatic field at $z_{sat} \simeq 19\lambda_w$ and $z \simeq 21\lambda_w$ (pointed by arrows in Fig.3(a)), where the radiation power becomes the peak value and the bottom one (Fig.5-(2) and (3)). Actually, the magnitude of $|f_{es}/f_p|$ is roughly estimated from Eq.(14) as $|f_{es}/f_p| \sim 0.9$ for $z_{sat} \simeq 19\lambda_w$ and $|f_{es}/f_p| \sim 1.7$ for $z \simeq 21\lambda_w$ by assuming $H(\psi,\psi_1) \simeq \langle \beta_{z0} \cos\psi_1 \rangle \sim 0.9$ and $\delta \sim 1.0$. At these axial coordinates, the periodic electron bounce motion is disturbed due to the strong electrostatic field. That is, some electrons become an untrapped state after one bounce motion owing to an irregular rotation of the bunched electron and obtain the kinetic energy from the ponderomotive potential as seen in Figs.5-(3) to (4). After that, the randomization of the bunched electron begins to take place(see Figs.5-(4) to (6)). Thus, the phase scrambling due to the randomization of the bunched electron leads the small amplitude oscillation of the radiation field and an increase of the up-scattering untrapped particle reduces the averaged radiation power.

Figure 6 illustrates the saturation efficiency η versus the beam current density I_b. The peak value of η, i.e. $\eta_{max}(\equiv P_{a,max} e/I_b E_b)$, and the averaged value $\langle \eta \rangle (\equiv \langle P_a \rangle / I_b E_b)$, are shown in both cases with and without the electrostatic field. It is found that both η_{max} and $\langle \eta \rangle \simeq \eta_{max}/2$ are scaled as $\eta \propto I_b^{1/3}$ in the absence of the electrostatic field, which coincides with the trapping argument[3,4]. The maximum conversion efficiency η_{max} for the $\phi \neq 0$ case roughly follows the same dependence as the $\phi = 0$ case, although the

slight deviation is observed for $I_b \gtrsim 0.5$KA/cm^2. Note here that in the presence of the electrostatic field, the averaged conversion efficiency $\langle\eta\rangle$ stays in the lower level than $\eta_{max}/2$ in the Raman regime for $I_b \gtrsim 0.1$KA/cm^2, roughly showing the scaling $\langle\eta\rangle \propto I_b^{1/5}$(dashed line in Fig.6). The conversion efficiency for B_0=1KG(axial guide field) and the corresponding fitting line($\langle\eta\rangle \propto I_b^{1/6}$) are also illustrated in Fig.6. It is found that the averaged efficiency becomes the lower value than that for the B_0=0 case, although η_{max} becomes almost same value as the B_0=0 case. According to the classification by H.P.Freund[9], the steady state particle orbit for B_0=1KG belongs to the Group I stable orbit. Thus, the averaged conversion efficiency is reduced by the electrostatic field in the high current Raman regime, providing the lower current density dependence $\langle\eta\rangle \propto I_b^{1/5\sim1/6}$ than the ideal case $\langle\eta\rangle \propto I_b^{1/3}$.

4.2 Effect of Axial Beam Energy Spread

In this subsection, we investigate the effect of the axial beam energy spread on a wave amplification over the wide range of the beam current density. An initial beam momentum distribution is given by the Gaussian type as $f_b(\boldsymbol{p})=n_b \exp\left[-(p_z-p_{z0})^2/\Delta p_z^2\right]\delta(p_x)\delta(p_y)/\pi^{1/2}\Delta p_z$, where $p_{z0}=\gamma_b mc(1-\gamma_b^{-1/2})^{1/2}$, and the momentum spread Δp_z is related to $\Delta\gamma_z$ through the relation $\Delta p_z=mc\Delta\gamma_z/\gamma_b(\gamma_b^2-1)^{1/2}$.

The dependence of the growth rate Γ and the energy efficiency η (both $\langle\eta\rangle$ and η_{max}) on the beam current density are shown in Figs.7 and 8 for $\Delta\gamma_z/\gamma_b$=2% in the presence of the electrostatic field. Same fitting lines as Figs.1 and 6 are also illustrated in Figs.7 and 8. It is found that both Γ and η are reduced compared with the $\Delta\gamma_z$=0 case in the low current Compton regime for $I_b \lesssim 0.1$KA/cm^2 and no considerable change is observed in the high current regime for $I_b \gtrsim 0.2$KA/cm^2. This comes from the fact that an axial energy spread produces an effect on the wave amplification when the axial

velocity spread $\Delta v_z = c^2 \Delta\gamma_z / \gamma_z^3 v_z$ becomes comparable to the phase velocity of the ponderomotive potential in the beam frame, i.e. $v_p - v_z \simeq c\omega_b / \gamma_z \gamma_b^{1/2} (k_+ + k_w)$ [13]. The critical beam density is written as

$$\xi \left(\equiv \frac{\omega_b}{\gamma_b^{1/2} k_w c} \right) \simeq \left(\frac{\Delta\gamma_z}{\gamma_z} \right) \frac{c(k_+ + k_w)}{v_z \gamma_z k_w} \equiv \xi_c \qquad (23)$$

For $\Delta\gamma_z/\gamma_z = 2\%$, the above relation corresponds to the current density $I_b \simeq 55\mathrm{A}$ ($\xi_c \simeq 0.075$), which agrees with the numerical calculation. Thus, the axial energy spread affects the wave amplification especially in the lower current operation regime.

In our analysis, however, the spatial evolution of the radiation power shows the different feature in two cases for $\Delta\gamma_z = 0$ and $\Delta\gamma_z \neq 0$ even in the high current region. Figure 9 shows the same spatial evolution as Fig.3(a) for $\Delta\gamma_z/\gamma_b = 0$ (a) and $\Delta\gamma_z/\gamma_b = 2\%$ (b) in the case of $I_b = 0.42\mathrm{KA/cm^2}$. Phase space plot of the particle distribution is also illustrated in Fig.10, corresponding to each spatial position of $z = 16\lambda_w$, $21\lambda_w$ and $z = 50\lambda_w$ in Fig.9. As already explained in §4-1, the amplitude oscillation is suppressed small in Fig.9(a) owing to the phase scrambling by the electrostatic force. On the other hand, the amplitude oscillation is recovered for the $\Delta\gamma_z \neq 0$ case as shown in Fig.9(b), although an averaged conversion efficiency provides almost same value as Fig.9(a). The recovery of the atrong amplitude oscillation is considered as follows. From the discussion in §2, the repulsive electrostatic force f_{es} is proportional to the phase factor $H(\psi, \psi_l) \simeq \langle \beta_{z0} \cos \psi_l \rangle$. The initial beam energy spread leads the phase space spread of the bunched electron in the ponderomotive potential well as shown in Fig.10(b)-(1) and (2)(compare with Fig.10(a)-(1) and (2)). Then, the value of $H(\psi, \psi_l)$ at around $\psi_l = 0$ becomes smaller than that for the ideal case of $\Delta\gamma_z = 0$ and the electrostatic force which induces the irregular rotation and

the randomization of the bunch electron is weakened(see Figs.10(a)-(3) and 10(b)-3). The reduction of the electrostatic field recovers the periodic electron bounce motion in the ponderomotive potential well, which leads the strong amplitude oscillation in the radiation field. Thus, the axial beam energy spread affects the spatial evolution of the radiation field even in the high current density region where Γ and η are not influenced.

5. Concluding Remarks

We investigated the effects of the longitudinal electrostatic field on the saturated energy conversion efficiency over the wide range from the lower current Compton regime to the higher current Raman one where the electrostatic force f_s becomes comparable to the ponderomotive force f_p. The bunched electron trapped in the ponderomotive potential suffers two times strong electrostatic forces at $\psi_1 \simeq 0$ during one bounce motion. It is found that the phase dependent electrostatic force $f_{es} \propto H(\psi, \psi_1)$ prevents the periodic bounce motion of the bunched electron especially in the strong Raman operation regime and increases the "up-scattering untrapped particle", with $S(\psi, d\psi/dz) > 0$ and $d\psi/dz > 0$, which removes the kinetic energy from the radiation field. Furthermore, the electrostatic field induces the phase mixing by scrambling the bunched electron in the ponderomotive potential well. Resultantly, the energy conversion efficiency averaged over the long wiggler distance $\langle \eta \rangle$ stays in a lower level than that expected from the trapping argument, providing the current density scaling $\langle \eta \rangle \propto I_b^{1/5} \sim I_b^{1/6}$. Furthermore, the amplitude oscillation of the radiation field is suppressed small. Note here that the strength of the amplitude oscillation is related to the fluctuation level of the output radiation power.

We also studied the effect of the axial beam energy spread. The axial beam energy spread $\Delta\gamma_z$ affects the linear growth rate of the radiation field Γ as well as the energy conversion efficiency η in the beam density ξ which

the randomization of the bunch electron is weakened(see Figs.10(a)-(3) and 10(b)-3). The reduction of the electrostatic field recovers the periodic electron bounce motion in the ponderomotive potential well, which leads the strong amplitude oscillation in the radiation field. Thus, the axial beam energy spread affects the spatial evolution of the radiation field even in the high current density region where Γ and η are not influenced.

5. Concluding Remarks

We investigated the effects of the longitudinal electrostatic field on the saturated energy conversion efficiency over the wide range from the lower current Compton regime to the higher current Raman one where the electrostatic force f_s becomes comparable to the ponderomotive force f_p. The bunched electron trapped in the ponderomotive potential suffers two times strong electrostatic forces at $\psi_l \simeq 0$ during one bounce motion. It is found that the phase dependent electrostatic force $f_{es} \propto H(\psi, \psi_l)$ prevents the periodic bounce motion of the bunched electron especially in the strong Raman operation regime and increases the "up-scattering untrapped particle", with $S(\psi, d\psi/dz) > 0$ and $d\psi/dz > 0$, which removes the kinetic energy from the radiation field. Furthermore, the electrostatic field induces the phase mixing by scrambling the bunched electron in the ponderomotive potential well. Resultantly, the energy conversion efficiency averaged over the long wiggler distance $\langle \eta \rangle$ stays in a lower level than that expected from the trapping argument, providing the current density scaling $\langle \eta \rangle \propto I_b^{1/5} \sim I_b^{1/6}$. Furthermore, the amplitude oscillation of the radiation field is suppressed small. Note here that the strength of the amplitude oscillation is related to the fluctuation level of the output radiation power.

We also studied the effect of the axial beam energy spread. The axial beam energy spread $\Delta\gamma_z$ affects the linear growth rate of the radiation field Γ as well as the energy conversion efficiency η in the beam density ξ which

is smaller than the critical one $\xi_c(\Delta\gamma_z)$. However, we found that the axial beam energy spread affects the spatial evolution of the radiation field even in the density region for $\xi \gtrsim \xi_c$. That is, the initial energy spread in an axial direction leads the phase space spread of the bunched electron in the nonlinear trapping stage and suppresses the repulsive electrostatic force. The reduction of the electrostatic force recovers the periodic electron bounce motion in the ponderomotive potential. Also recovered the strong amplitude oscillation of the radiation field following the periodic electron bounce motion. Thus, the strength of the amplitude oscillation closely related not only to the beam current density I_b but also to the magnitude of the axial energy spread $\Delta\gamma_z$.

In the present numerical calculation, we fixed the wave frequency to f=60GHz. We also obtained the similar reduction of the averaged conversion efficiency in the wide range of the exciting wave frequency. Here, we employed a spatially 1-dimensional code which is useful for studying the basic process treated in this paper. However, 2-dimensional effects such as the beam emittance, i.e. the momentum spread in the $p_\perp$-direction, and the selective excitation of the wave guide mode[14,15] are not included in the preset model.

In the calculation, we considered the constant parameter helical wiggler. Results obtained here will affect the energy conversion efficiency for the tapered wiggler FEL, where the trapping efficiency is an essential problem. It should be also noted that the axial beam energy spread as well as the electrostatic field will influence the side-band instability because the amplitude oscillation of the radiation field becomes a free energy source for various parastic wave excitations.

Acknowledgment

We are grateful to Drs. K.Ohasa, K.Hoshino and T.Ogawa for their fruitful discussions and comments. We wish to express sincere thanks to Drs. K.Mima and S. Kuruma of Institute of Laser Engineering of Osaka University and Dr. T.Taguchi of Setsunan University for their useful discussions. Thanks are also due to Dr. T.Takeda and Dr. M.Tanaka for their continuous encouragement.

References

1). T.J.Orzechowski et al., Phys.Rev.Lett. 32, 2172(1986).

2). S.H.Gold et al., Phys.Fluids 27, 746(1984).

3). P.Sprangle and R.A.Smith, Phys.Rev.A21, 293(1980). P.Sprangle, R.A.Smith and V.L.Granatstein : Infrared and Millimeter Waves, edited by K.J.Button(Acdemic Press, 1979) Vol.1, p.279.

4). P.Sprangle, Cha-Mei Tang, and W.M.Manheimer, Phys.Rev.A21, 302(1980).

5). H.P.Freund and H.Bluem, and C.L.Chang, Phys.Rev.A36, 2182(1987).

6). H.P.Freund, Phys.Rev.A37, 3371(1988).

7). T.M.Antonsen, Jr, Phys.Rev.Lett.58, 211(1987).

8). N.M.Kroll, P.L.Moton, and M.N.Rosenbluth, IEEE J.Quantum Electron 17, 1436(1981).

9). H.P.Freund, Phys.Rev.A27, 1977(1983).

10). M.Shiho, K.Hoshino, Y.Kishimoto, et al. "Recent Result and future plan of the JFT-2M tokamak ECRH experiment", to be published in the Proc. of the IAEA Technical Comittee Meeting on ECE and EC-7 Meeting, May 1989, Hefei, China.

11). Y.Kishimoto and H.Oda, "1-Dimensional Single-Mode Nonlinear Free Electron Laser(FEL) Amplification Code", JAERI-M 89-061(1989).

12). It is found form the theory for the linear response in Ref.3 that the transition from Compton regime to Raman one takes place at the beam density $\xi=\gamma_{z0}^3 a_0^2/16\gamma_b^2$. The relation corresponds to $I_b \simeq 50 A/cm^2$ for the present numerical calculation and roughly agrees with the transition current density obtained in Fig.1.

13). S.Kuruma and K.Mima, J.Phys.Soc.Jpn.55,1122(1986).

14). A.K.Ganguly and H.P.Freund, Phys. Fluids 31, 387(1988).

15). H.P.Freund and A.K.Ganguly, Phy.Rev.A34,1242(1986).

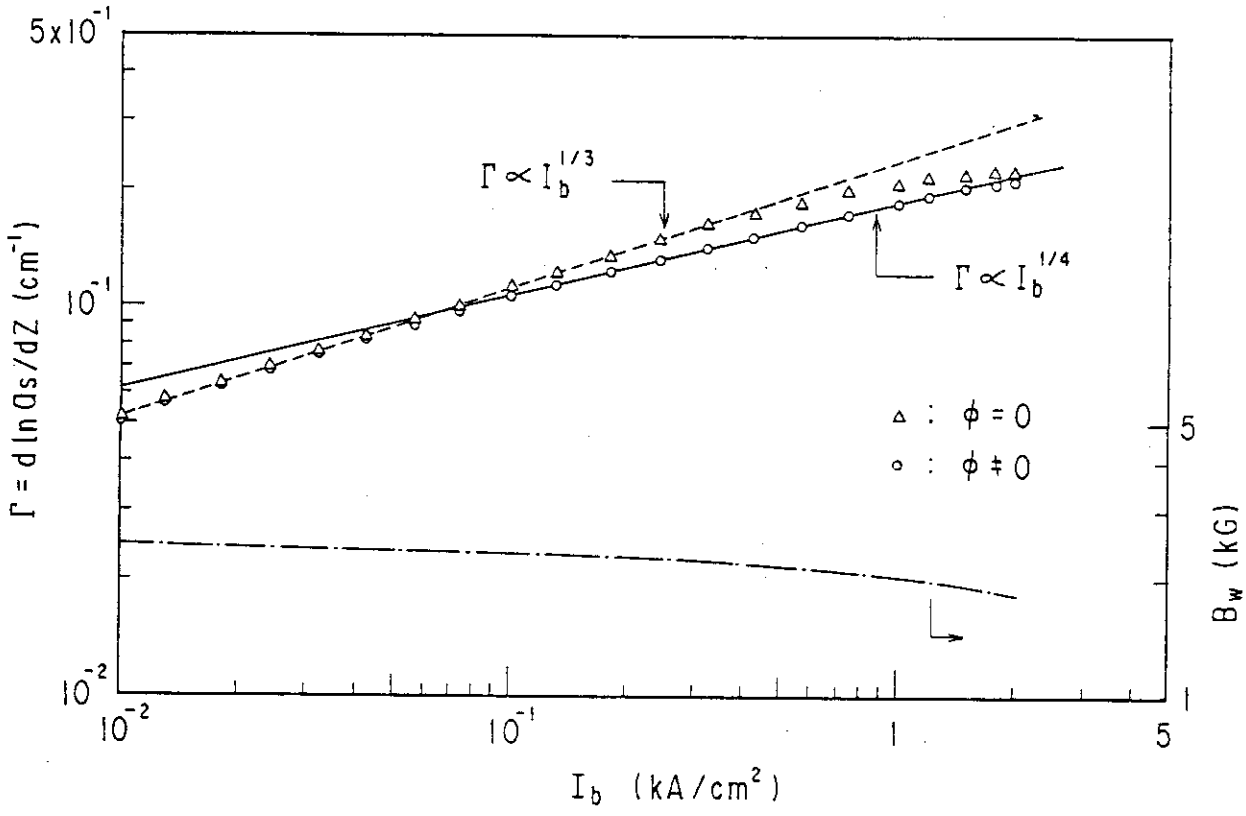

Fig.1 Dependence of the linear growth rate Γ on the beam current density I_b in the case without electrostatic field(open triangle) and with one(open circle). Parameters are f=60GHz, E_b=1MeV, λ_w=4cm and no axial guide field is applied(B_0=1KG). Dependence of the wiggler field B_w on I_b is also illustrated by dash dotted line. Dashed and solid line represent $\Gamma=0.235 I_b^{1/3}$ and $\Gamma=0.185 I_b^{1/4}$, respectively.

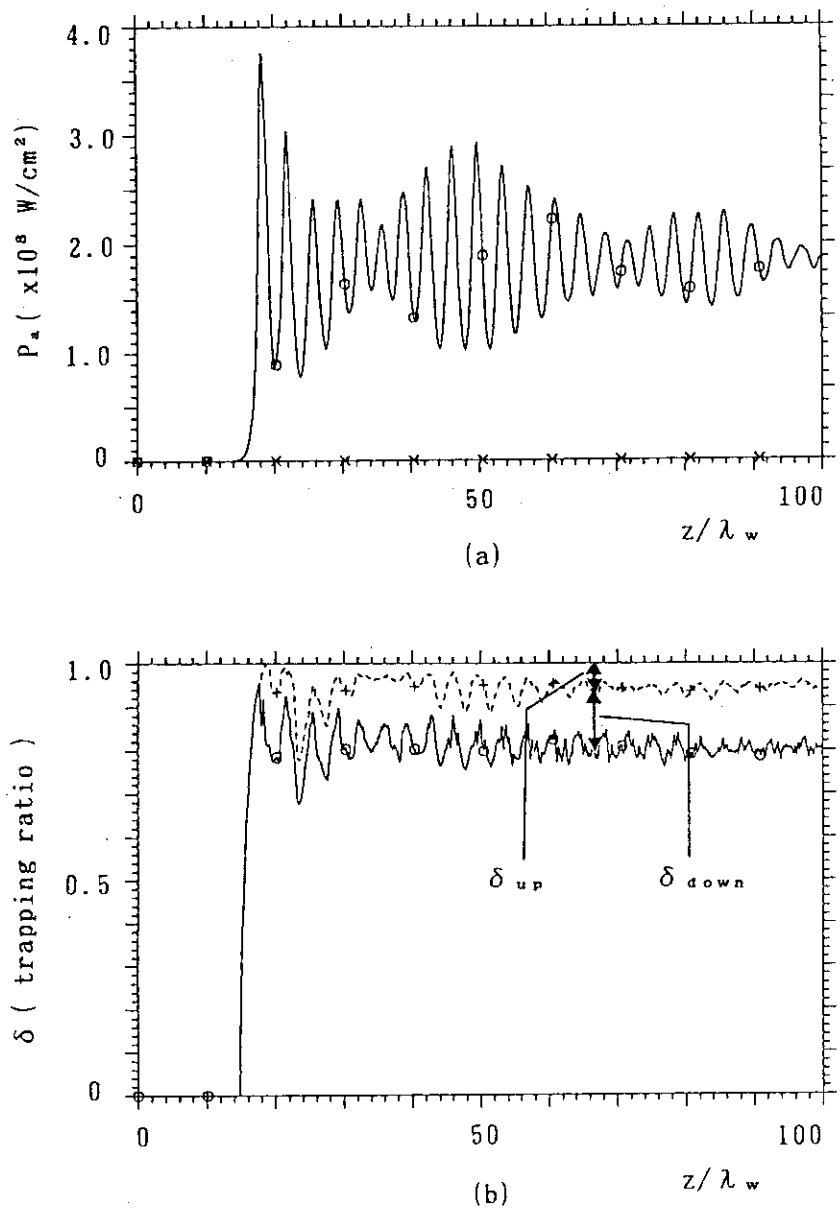

Fig.2 Radiation power density P_a (a) and trapped/untrapped particle ratio, i.e. η and $1-\eta$ (b), as a function of the axial distance in the absence of electrostatic field for I_b=1.5KA/cm^2 and B_w=1.94KG. Other parameters are same as Fig.1. Untrapped particle ratio $1-\eta$ is devided into the up-scattering particle ratio η_{up} and the down-scattering one η_{down}.

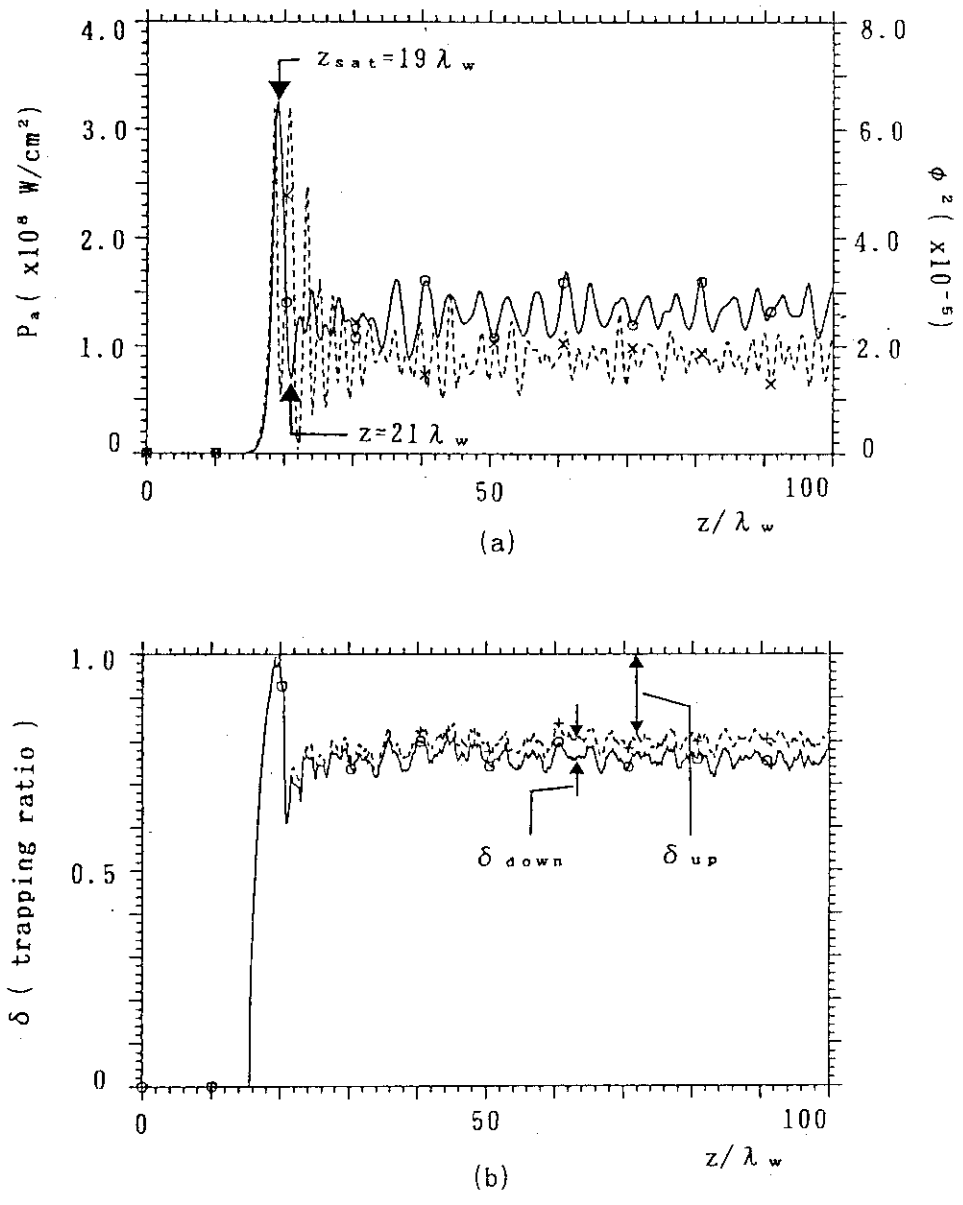

Fig.3 (a) Radiation power density P_a and (b) trapped/untrapped particle ratio, i.e. η and $1-\eta$ (b), as a function of the axial distance in the presence of electrostatic field for I_b=1.5KA/cm^2 and B_w=1.94KG. Other parameters are same as Fig.1. Dashed line in Fig.3(a) represents the electrostatic field ϕ^2.

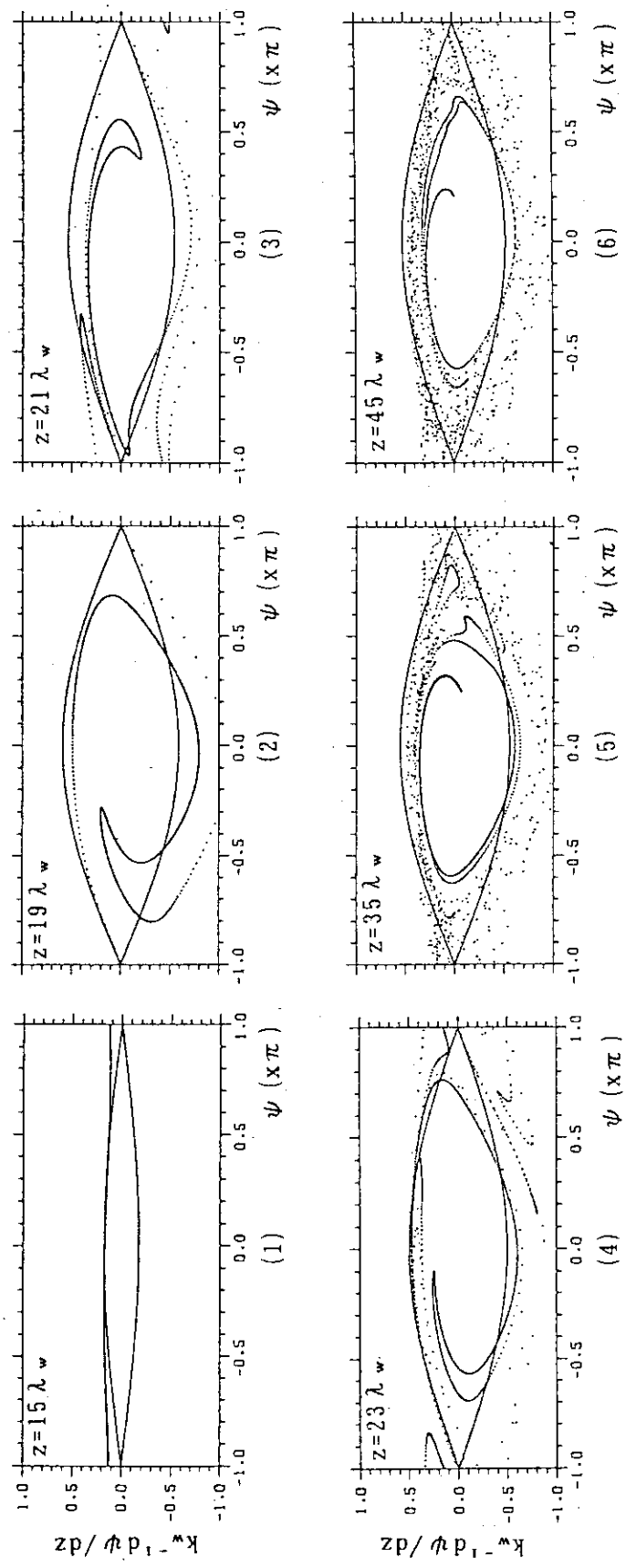

Fig.4 Phase space plot of $(d\psi/dz)k_w^{-1}=(k_+/k_w)+1-\omega/v_z k_w$ for various axial positions corresponding to Fig.2. Solid line represents the separatrix.

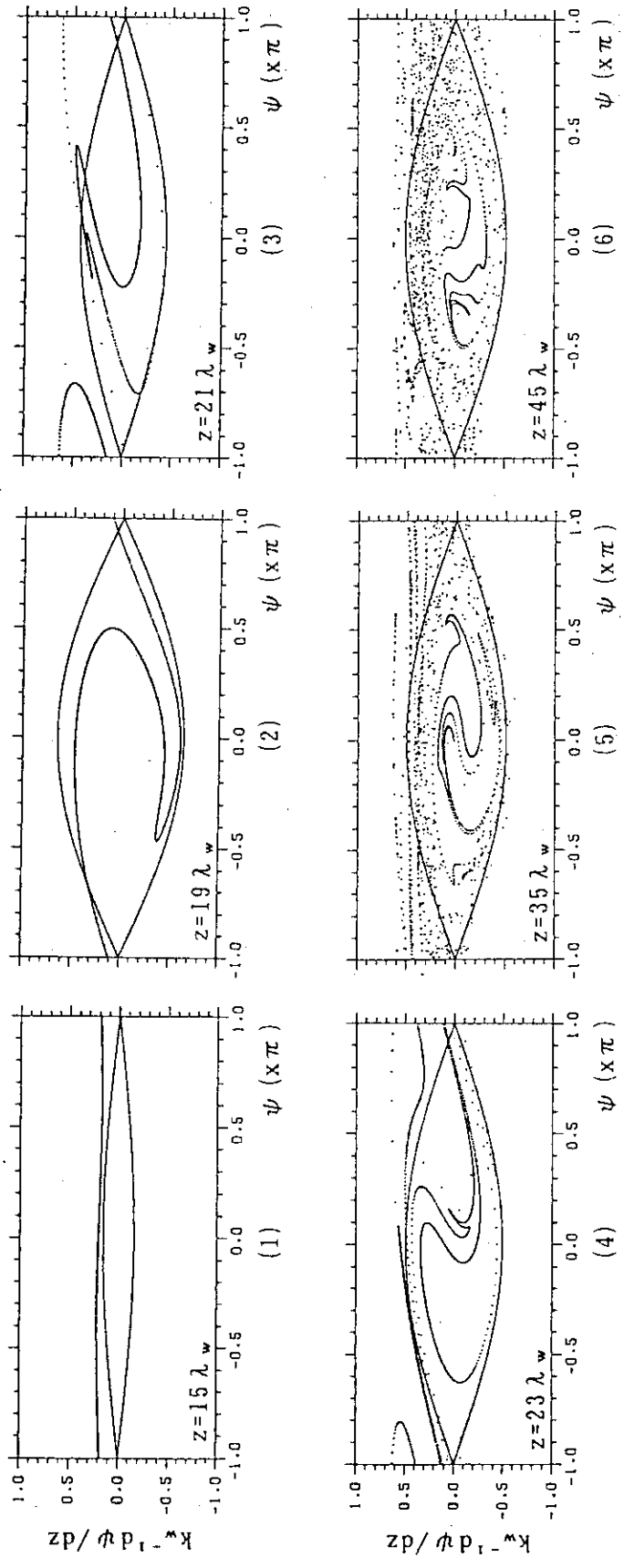

Fig.5 Phase space plot of $(d\psi/dz)k_w^{-1}=(k_+/k_w)+1-\omega/v_z k_w$ for various axial positions corresponding to Fig.3.

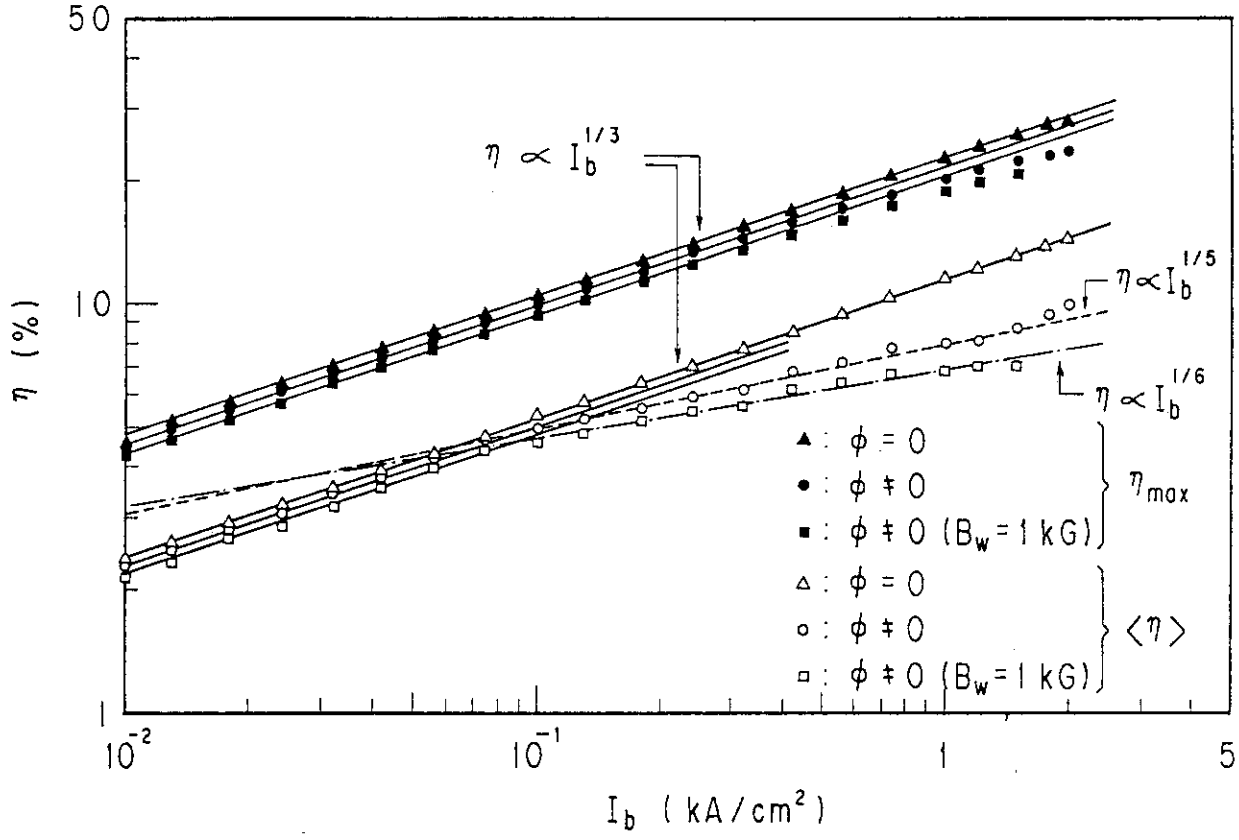

Fig.6 Dependence of the maximum energy conversion efficiency η_{max} and the averaged one $\langle\eta\rangle$ on the current density I_b for cases with (circle) and without (triangle) the electrostatic field. Parameters are same as Fig.1. Squares represent the case for B_0=1KG(axial guide field) in the presence of the electrostatic field. Fitting lines given by $\eta \propto I_b^{1/3}$, $\eta \propto I_b^{1/5}$ and $\eta \propto I_b^{1/6}$ are also illustrated, corresponding to each current dependence.

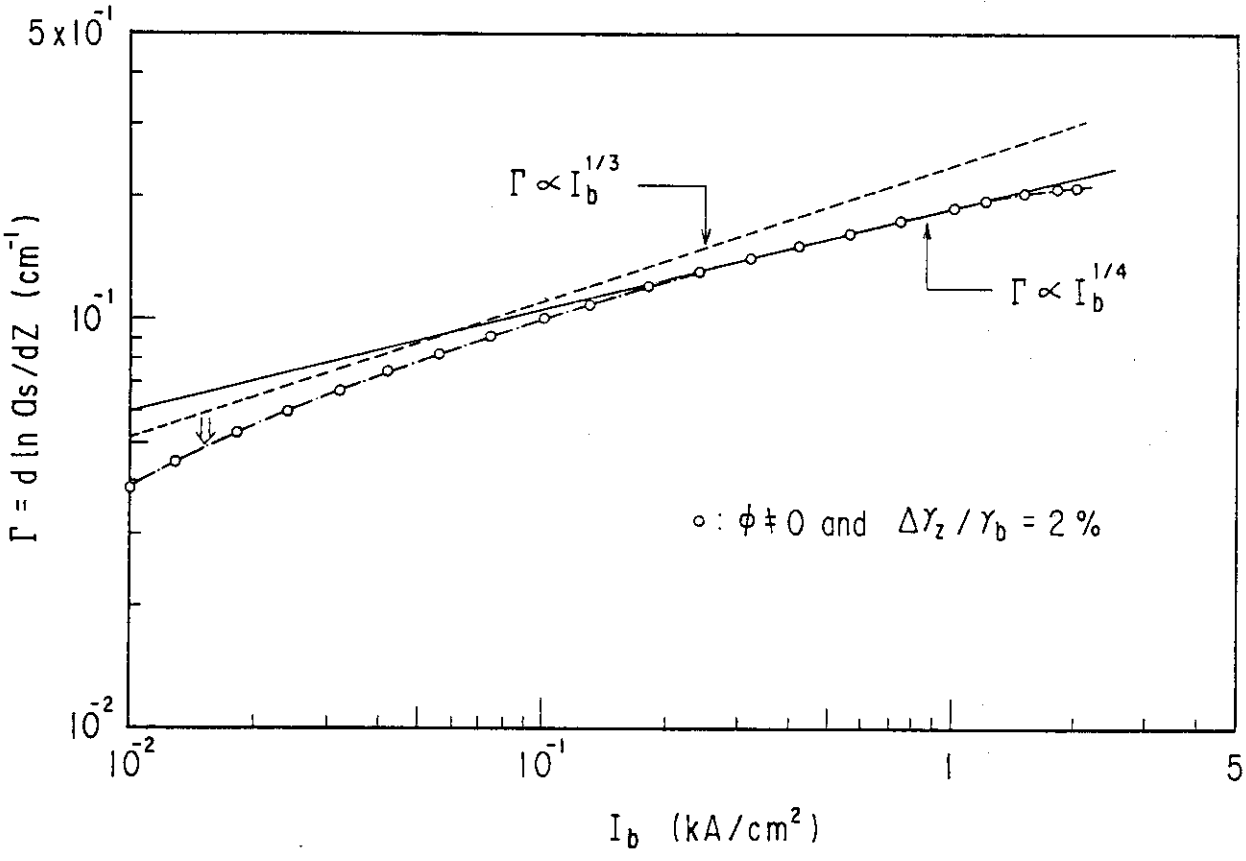

Fig.7 Dependence of the linear growth rate Γ on the beam current density I_b in the presence of the electrostatic field for $\Delta\gamma_z/\gamma_b$=2%. No axial guide field is applied(B_0=1KG). Dashed and solid line represent $\Gamma=0.235I_b^{1/3}$ and $\Gamma=0.185I_b^{1/4}$, which are same lines as Fig.1.

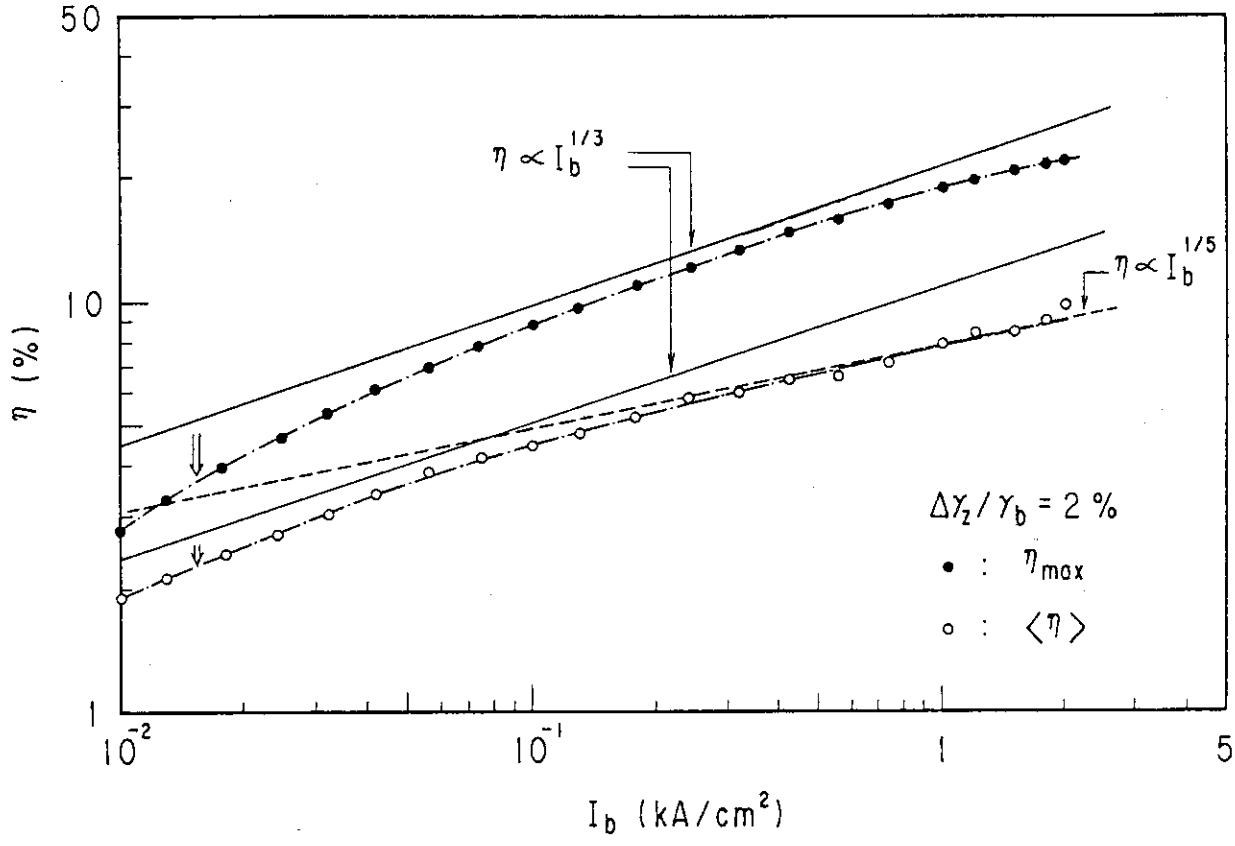

Fig.8 Dependence of the maximum energy conversion efficiency η_{max} and the averaged one $\langle\eta\rangle$ on the current density I_b in the presence of the electrostatic field for $\Delta\gamma_z/\gamma_b$=2%. Fitting lines for $\Delta\gamma_z$=0 in Fig.6, i.e. $\eta \propto I_b^{1/3}$ and $\eta \propto I_b^{1/5}$, are also illustrated.

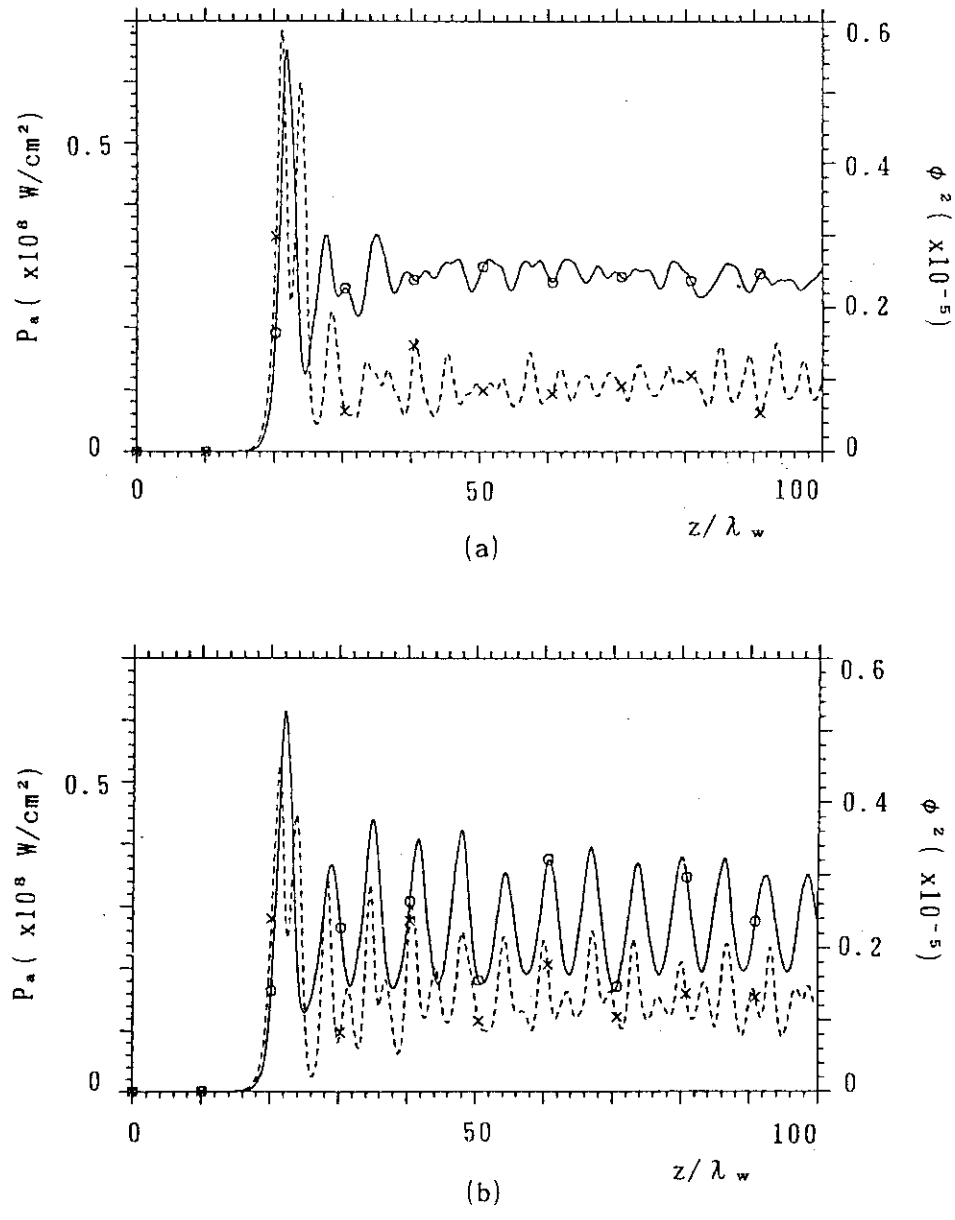

Fig.9 Radiation power density P_a and electrostatic field ϕ^2 as a function of the axial distance in the presence of the electrostatic field for $\Delta\gamma_z/\gamma_b=0$ (a) and $\Delta\gamma_z/\gamma_b=2\%$ (b). Beam current density is $I_b=0.42\mathrm{KA/cm^2}$.

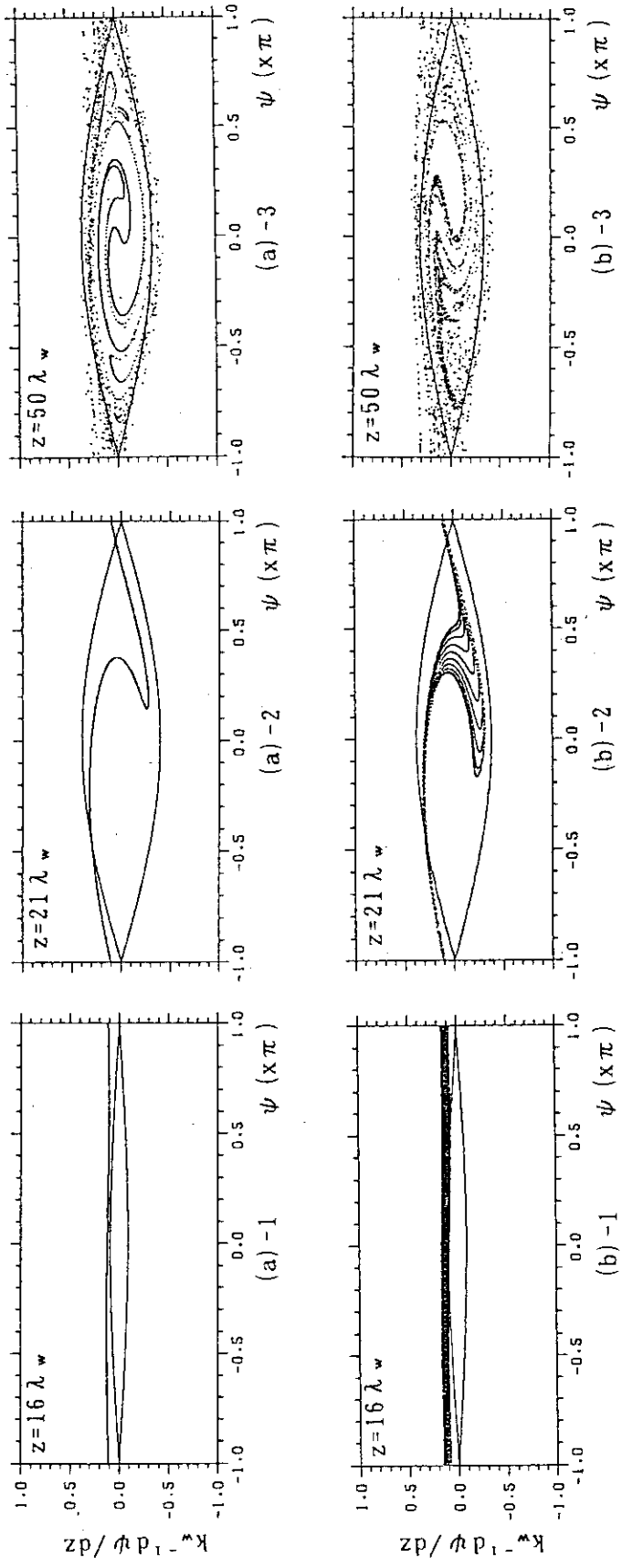

Fig.10 Phase space plot of $(d\psi/dz)k_w^{-1}=(k_+/k_w)+1-\omega/v_z k_w$ in the presence of the electrostatic field for $\Delta\gamma_z/\gamma_b=0$ (a) and $\Delta\gamma_z/\gamma_b=2\%$ (b), corresponding to each axial position in Figs.9(a) and (b).